IEEE Access
Multidisciplinary | Rapid Review | Open Access Journal

Date of publication xxxx 00, 0000, date of current version xxxx 00, 0000.

Digital Object Identifier xxxx

Design, Construction, and Rough-Terrain Locomotion Control of Novel Hexapod Walking Robot with Four Degrees of Freedom per Leg

PETR ČÍŽEK, MARTIN ZOULA, and JAN FAIGL
[1]Authors are with the Czech Technical University in Prague, Faculty of Electrical Engineering, Technicka 2, 166 27, Prague, Czech Republic
Corresponding author: Petr Čížek, (e-mail: petr.cizek@fel.cvut.cz).

The presented work has been supported by the Czech Science Foundation (GAČR) under research project No. 18-18858S.

ABSTRACT Multi-legged walking robots are suitable platforms for unstructured and rough terrains because of their immense locomotion capabilities. These are, however, redeemed by more sophisticated control and energy-demanding motion in comparison to wheeled robots. Particularly, electrically actuated multi-legged walking robots suffer from the adverse ratio between the robot body weight and payload capacity. Moreover, the ratio of the locomotion speed and endurance is far from what can be achieved with wheeled robots. In this paper, we focus on six-legged walking robots with statically-stable gait. Based on the analysis of existing solutions, we propose a novel construction of the affordable electrically actuated robot with substantial improvements in its motion capabilities, locomotion speed, reliability, and endurance. The proposed design is implemented in a Hexapod Ant Robot (HAntR) that is accompanied by the developed locomotion control approach to improve its rough terrains negotiation capabilities by the active distribution of the robot weight to the legs in the stance phase. Properties of the robot have been experimentally verified in extensive deployments, and based on the experimental benchmarking of the built prototype, HAntR is capable of locomotion for over an hour with the payload of 85% of its weight, and its maximum crawled distance per one second is 87 % of its nominal length. HAntR represents significant improvements not only regarding the robots with identical actuators but also in comparison to other existing platforms. Therefore, we consider the robot HAntR represents a step further towards a wide range of future applications and deployments of six-legged walking robots.

INDEX TERMS Multi-Legged Robot, Locomotion Control, Rough Terrains, Robot Design

I. INTRODUCTION

MULTI-LEGGED robots are known to outperform wheeled and tracked platforms in rough terrains operations [1]. Specifically, six-legged (hexapod) walking robots can be characterized by their fault-tolerance for walking on unstructured terrain [2] that can be experienced in various missions such as exploration [3], mine detection in wild [4], or even data collection missions in extreme environments [5]. However, it all comes at the cost of relatively complex mechanical construction and locomotion control. On top of that, multi-legged robots and specifically electrically actuated platforms suffer from high energy consumption, which is also required for the stance phase, due to the walker's inherent need for actively supported limbs. Therefore, three main research streams can be identified in the literature to improve the properties of the multi-legged robots by novel actuators, robot morphology, and locomotion control strategies [6]. For example, the quadruped robot ANYmal utilizes series elastic actuators [7], while the MIT Cheetah 3 [8] uses direct drive actuators and it has the lowest reported Cost of Transport (CoT) of 0.45 for trotting. Similarly, for six-legged robots, various actuators and leg mechanisms have been proposed, such as those within the RHex project [9] or more recent amphibious robotic platforms, e.g., X-RHex [10]. In this paper, we are, however, focused on statically stable six-legged robots [11] with the traditional leg design based on electrically actuated joints because of our interest in capabilities to negotiate individual footsteps under challenging

conditions.

The power consumption of multi-legged robots can be decreased by the specific robot morphology [12] and leg design [13], [14], but also by locomotion control [4], gait parametrization [15], and foot contact force optimization with further explicit planning the robot trajectory together with the suitable footholds as presented by Belter et al [16]. Regarding the shape of the robot and leg configuration, legs distributed axi-symmetrically around the body with a hexagonal or circular shape, such as robots LEMUR [5] and Crabot [17], in general, better support weight distribution than side-symmetrical robots of rectangular shape [18]. However, rectangular-shaped robots, which are inspired by insects with six legs, can exhibit relatively fast forward locomotion at the cost of decreased flexibility in turning sideways [19]. Therefore, specific energy-efficient locomotion gaits are studied not only for walking [20], [21] but also for turning motion [22].

One of the main issues of the existing electrically-actuated six-legged walking platforms is the adverse ratio between the robot weight and payload capacity that is also related to the relatively short endurance on battery and slower locomotion in comparison to the wheeled robots during the operation on flat terrains. The issues are closely related to the robot morphology, leg design, and mechanical construction of the robot. In this sense, we analyzed the main influencing factors of the existing solutions, including our experience with hexapod walking robots [23], and we propose a novel robot design to improve the aforementioned characteristics of multi-legged walking robots. In particular, we aimed to address motion capabilities, locomotion speed, payload capacity, and robot endurance by considering possible approaches with their pros and cons.

Although the characteristics are mutually dependent, and all of them are related to the energy demands, *motion capabilities* in rough and unstructured environments are prominent properties of multi-legged robots. Ruggedized construction and simplified morphology [9] increase the robustness of the robot, which may improve the rough terrain locomotion capabilities up to some extent, but sacrifice the negotiation of individual footsteps in challenging terrains. Contrarily, more degrees of freedom (DoF) in robot morphology improve maneuverability by allowing the robot to distribute its weight [24], [25]. On the other hand, additional actuators usually result in increased power demands, also cased by increased weight.

Locomotion speed is a crucial property specifically for operation in large-scale environments. In general, it is mostly influenced by the achievable leg swing length given by the robot morphology, the dynamics of the leg, and the locomotion control approach. Here, we need to take into account that the increased swing length implies higher torques in joints that further influence the power consumption and payload capacity of the robot.

Payload capacity is essential to ensure sufficient capacity for computational, sensory, and communication equipment

FIGURE 1. The prototype of the HAntR during the deployment in the cave environment.

needed for achieving the desired level of robot autonomy. Although massive robots with payload in hundreds of kilograms have been developed [11] such as ATHLETE with the reported capacity of $450\,\mathrm{kg}$ [26], we focus our research on small hexapod walking robots with dimensions in tens of centimeters and weight of units of kilograms similar to Crabot [17], Messor II [27], Weaver [25] to name few here. Especially for small robots, the influence of the payload to joint torques, weight distribution, and thus power consumption and endurance, is still one of the fundamental questions of the suitable robot design.

Finally, the *robot endurance* is also the property of our interest that depends on the battery capacity to cover the power consumption of the robot. There is a trade-off between the available capacity and weight of the battery, but from the mission point of view, the endurance is also related to the speed of the robot. Even relatively slow robots can achieve long travel distances with sufficient endurance as it was reported more than 25 years ago for the robot Ambler [28] with the locomotion speed $0.4\,\mathrm{m}$ per one minute but with the endurance over 21 hours. In our design choices, we aim to increase the endurance of the robot. At the same time, we also aim to increase (or at least preserve) the robot motion capabilities, payload, and locomotion speed in comparison to existing solutions.

Based on the made qualitative and quantitative analysis, we propose a novel mechanical and control design of the six-legged walking robot to address the aforementioned characteristics. In particular, the proposed mechanical design comprises a densely packed symmetric body that hosts the control electronics and six legs, each with four actuated joints. The introduced four DoF per leg directly improves the motion capabilities and allows for improved balance control of the robot, which positively influences the mass distribution between individual legs during the locomotion on sloped surfaces or contour lines. The achieved mass distribution, in turn, lowers the joint torques and improves the endurance of the robot. Furthermore, a complete locomotion control

scheme, built on the previous work [23], allows the robot to negotiate rough terrain blindly while maintaining smooth body motion.

Following the made design choices, a prototype of the robot named Hexapod Ant Robot (HAntR) has been built (see Fig. 1) to experimentally verify the proposed design and report on benchmark evaluation of the robot capabilities accompanied with the developed locomotion control strategy. Both the comparison with the existing platforms and experimental evaluation support the developed prototype robot improves characteristics of the small electrically-actuated hexapod walking robots. The HAntR is capable of locomotion over an hour with the payload of $85\,\%$ of its weight, and its maximum crawled distance per second is about $87\,\%$ of its nominal length.

The paper is organized as follows. An overview of the most related existing six-legged robotic platforms with their main characteristics is listed in the following section together with a brief discussion and comparison of the developed prototype robot with the most similar six-legged walking robots. Section III details the proposed mechanical construction considerations involved in the design of the novel hexapod robot. The proposed locomotion control strategy is presented in Section IV. Results on the real experimental deployments and benchmarking the built prototype robot are reported in Section V. Concluding remarks are dedicated to Section VI.

II. RELATED WORK

Among existing multi-legged platforms, six-legged robots have an exclusive status as six legs is the smallest number of legs to offer two-stride statically stable gait. The presented research results are motivated by the deployment of relatively small platforms (about tens of centimeters in diameter) in robotic information gathering missions, where robots are requested to autonomously collect measurements in rough and unstructured terrains, which impose requirements on robotic platforms. In particular, the payload and power capabilities of the robot have to support sufficient computational power to enable computationally intensive processes of autonomous exploration [29], [30], while maintaining locomotion speed of the platform for an extended period, i.e., to explore up to hundreds of meters large environments.

The existing research and commercially available hexapod walking robots range from miniature, cockroach-like robots with piezo actuators [31], up to heavy duty robots [32] including large marine platforms for underwater inspection [33]. In the following summary of the literature review with a comparison to the proposed HAntR platform, we present only platforms reported for being used or being considered for autonomous exploration. Besides, we do not aim to provide an exhaustive review of all existing designs of six-legged walking robots. Instead, we focus on relatively new small platforms with electric actuators.

Many of the developed rectangular-shaped hexapod walking robots are inspired by natural archetypes such as ants, cockroaches [31], or beetles [34] that use three DoF per leg. These include research platforms like Messor II [27], DLR-Crawler [35], Corin [36], Alpha [34], MORF [37], and Snake Monster [38], but also commercial platforms PhantomX AX [39], MX Phoenix [40], and Daisy [41]. All these platforms are only able to control the position of the leg foot-tip, while the disaster response robot LAURON V [42], extraterrestrial Crater Explorer (CREX) [3], and recently introduced Crabot [17] rely on the 4-DoF leg design. Finally, the most complex robot is Weaver [25] with 5-DoF legs. It has been shown that the fourth and fifth DoF leg kinematic chains improve the maneuverability of the robot [24], [25] and supports manipulation tasks [3], [42] at the cost of more complicated mechanical design, and subsequently increased mass and power consumption of the robot.

On the other hand, high terrain mobility can be achieved even with a single DoF per leg as it is demonstrated by robots from the RHex family [9], [43]. However, the RHex robot cannot rely on precise locomotion control, as it is not capable of negotiating individual footsteps [44] or optimize its posture [36], which is essential in heavily cluttered terrains.

Therefore, for the HAntR, we followed the research streams with increased DoF and opted for the 4-DoF leg design as a suitable trade-off between the 3-DoF design that has lower motion capabilities and 5-DoF leg used with the Weaver robot [45]. Although 5-DoF leg design [45] allows for precise control of the leg endpoint contact angle, there is still sheer force exerted during the stance phase as the body of the robot moves forward. Besides, the fifth actuator presents an additional payload, increased power consumption, and, most importantly, it also influences the leg dynamics.

Robot morphology needs to be supported by appropriate locomotion control to exploit the maneuverability of the robot in hexapedal locomotion in challenging terrains. As one of the research streams, biologically inspired neural networks including CPGs [47], [48] are widely used for control of multi-legged robots like Alpha [34] or MORPH [37] which has been designed specifically as a modular testbed for locomotion control strategies. On the other hand, the robot motion can be governed by deliberative control strategies including blind locomotion control [23] or precise foothold planning based on exteroceptive sensing [44]. Nevertheless, the tactile sensing is required as a part of the control approach for successful foothold adaptation in challenging terrains.

Among a wide range of control approaches, foothold adaptation based on online force estimation using direct measurements of the joint forces by dedicated sensors [42], [49]–[51], or based on the estimation of joint torques using servomotors current readings [45], [52] are utilized in existing solutions. However, in our design choices, we have been limited to the usage of the Dynamixel AX-12A servomotors that do not directly provide the information about the motor current, and thus the joint torque. In such a case, foot-contact detection methods can be employed using tactile sensors [27], or pressure sensors [53] at the leg foot-tips. However, these methods require wired connection per each leg in addition to the control bus of the servomotors, which is more prone to

TABLE 1. Comparison of hexapod platforms

Platform	DoF†	Size‡ LxWxH [m]	Mass [kg]	Battery cap. [W h]	Energy density [W h kg^{-1}]	Operation time♮ [h]	Maximum speed♮ [m s^{-1}]
X-RHex [43]	6	$0.6 \times 0.3 \times 0.1$	9.5	288.0	30.3	3.0	1.54
AmphiHex-II [10]	6	$0.5 \times 0.3 \times 0.1$	14.0	576.0	41.2	-	-
PhantomX AX [39]	18	$0.5 \times 0.5 \times 0.2$	2.6	48.0	18.5	2.0	0.29
Messor II [27]	18	$0.5 \times 0.5 \times 0.2$	2.6	cable	-	-	-
DLR Crawler [35]	18	$0.5 \times 0.5 \times 0.2$	3.5	cable	-	-	0.20
MORF [46]	18	$0.4 \times 0.6 \times 0.3$	4.2	128.7	30.6	1.5	0.70
Corin [36]	18	$0.5 \times 0.6 \times 0.2$	4.6	cable	-	-	0.10
Snake Monster [38]	18	$0.7 \times 0.7 \times 0.3$	4.6	cable	-	-	-
MX Phoenix [40]	18	$0.8 \times 0.8 \times 0.3$	4.8	74.0	15.4	-	>0.50
Daisy [41]	18	$1.1 \times 1.1 \times 0.4$	21.0	98.0	4.7	>2.0	0.13
HAntR (Proposed)	**24**	$\mathbf{0.5 \times 0.5 \times 0.3}$	**2.9**	**66.6**	**23.0**	**>1.0**	**0.43**
Crabot [17]	24	$0.7 \times 0.7 \times 0.3$	3.2	28.7	9.0	0.2	0.05
Lauron V [42]	24	$0.9 \times 0.8 \times 0.7$	42.0	355.2	8.5	>2.0	-
CREX [3]	26	$0.8 \times 1.0 \times 0.2$	23.0	177.6	7.7	1.3	0.17
Weaver [25]	30	$0.6 \times 0.6 \times 0.3$	7.0	118.4	16.9	∼1.0	0.16

† Number of controllable DoF.
‡ Outline of the robot when standing in the default configuration.
♮ Listed values (if known) are reported in the respective cited publications.

damage and failure during rough terrain locomotion. Besides, they allow tactile sensing only at the leg foot-tip whereas the contact can occur anywhere along the leg morphology. Hence, a minimalistic approach for foot-contact events detection has been adapted based on the approach [23] with the same servomotors. The method utilizes only the position feedback of the Dynamixel AX-12A servomotors to monitor the virtual elasticity in the joints. Hence, we employed the method for HAntR foothold adaptation as it requires no additional sensors for terrain negotiation that can be thus achieved only by the affordable servomotors themselves.

Although the proposed robot design with 4-DoF legs utilizes the same servomotors as the PhantomX AX robot [39] with 3-DoF per leg, it is only about $0.3\,\mathrm{kg}$ heavier despite having six additional actuators. Here, it is worthy of noting that Crabot [17] is the most similar to our design, but the trunk of the Crabot is less compact, and the leg morphology is of the PhantomX AX robot with a single prepended servo in the kinematic chain. The design choice of Crabot thus makes the kinematic chain of the leg twice as long, and thus the robot operates in a wide straddle (as opposed to our proposed solution) which results in Dynamixel AX-12A servomotors failing to support the robot own mass. Therefore, the authors of the Crabot platform had to use stronger Dynamixel AX-18A servomotors [17], while our design works with the less powerful AX-12A series.

Based on the review of the existing six-legged walking robots, we collect their main characteristics and list them in Table 1 ordered according to the DoF of the platform legs and robot mass. In the comparison to existing platforms, the proposed HAntR is one of the smallest because of the packed design of the robot trunk. Besides, it is also light, which is most likely because of the 3D-printed mechanical parts. Finally, HAntR has one of the highest energy densities and locomotion speeds among the listed platforms. The particular design choices are detailed in the next section that is followed by a description of the employed locomotion control strategies in Section IV. The experimentally verified achieved characteristics are reported in Section V.

III. MECHANICAL DESIGN

The design of the HAntR is inspired by the existing solutions and also based on the five years of experience with the PhantomX AX robot [39] to enhance its kinematic capabilities and improve its operational characteristics, especially the locomotion speed and endurance. In this section, we share the ideas behind mechanical design choices and the proposed solution. Besides, to make the paper self-contained, the formulation of the forward kinematics task (FKT) and inverse kinematics task (IKT) is in Section III-B and Section III-C, respectively. The presented formulation of the IKT in the global reference frame significantly simplifies the locomotion control approach presented in Section IV.

A. DESIGN CHOICES AND PROPOSED SOLUTIONS

The robot body and legs have been designed with the focus on the overall weight reduction and improved kinematic capabilities in comparison to the PhantomX AX robot [39], and the resulting design is visualized in Fig. 2a. The leg design follows the bio-inspired nomenclature for joints that are named *coxa*, *trochanter*, *femur*, and *tibia* according to their placement with respect to the body and previous links as it is visualized in Fig. 2c.

Multiple configurations have been considered for the design of the fourth DoF of the leg. We have rejected the yaw-roll-pitch-pitch configuration employed in the design of

(a) Robot render. (b) Body render. (c) Leg structure.

FIGURE 2. (a) Render of the HAntR. Custom-designed parts that have been 3D-printed are colored in blue. (b) Dismantled view of the robot body with visualization of the battery pack. (c) 4-DoF leg design with distinguished kinematic links (black-torso, red-coxa, green-trochanter, blue-femur, yellow-tibia).

Weaver [25] because the trochanter joint needs an extended body area for its operation. Such a solution would not leave enough space in the body for batteries and electronics, and the body would be unnecessarily high, which negatively influences the body inertia and the vertical position of the center of mass. We have also considered the yaw-pitch-roll-pitch configuration as it is employed with the four-legged Pleurobot [54]. However, such a configuration puts a considerable load on the femur servomotor, and it negatively influences the leg dynamics by putting heavy servomotors further from the body. Therefore, we have selected the roll-yaw-pitch-pitch configuration as it is employed with Lauron V [42] and Crabot [17], but we have reconsidered the servomotors placement to reduce the overall size of the robot, enhance the leg dynamics, and simplify the kinematics tasks. In particular, the coxa servomotors are placed in a symmetric hexagonal pattern as close as possible to each other, see the visualization in Fig. 2b.

We have decided on the symmetrical body of the robot, designed with six axes of planar symmetry, to support weight distribution. Thus, identical kinematics, statics, and dynamics are applied on all the legs, which further simplifies the control strategy. Besides, the free area between the coxa servomotors also leaves space for electronics and batteries. In our case, we primarily target to use the area for six 18650-type Lithium-Ion batteries (see Fig. 2b) in the 3S-2P configuration. The assembled battery pack has $11.1\,\mathrm{V}$ nominal voltage, $30\,\mathrm{A}$ discharge current, and $6\,\mathrm{A\,h}$ capacity, while weighting only $288\,\mathrm{g}$. The battery pack fits perfectly the area between the servos, which improves the mass distribution of the robot that is concentrated towards the vertical axis of the symmetry, and reduces the inertia of the robot body. Notice, the outer area between the servomotors can fit additional six 18650-type batteries, which can further extend the overall battery capacity to $12\,\mathrm{A\,h}$, and thus prolong the operation time of the robot beyond two hours. The free space above and between the servos may be used to fit a custom electronic control board and sensors.

The other servomotors are placed such that the coxa and trochanter have intersecting rotation axes. Further, the femur and tibia servomotors are placed to maintain a compact design that has been shown to reduce the overall inertia of the robot leg [55]. Such a design choice lowers the stress put on the individual servomotors, leaving the distant parts like femur and tibia lightweight. For the same reason, the tibia link is crafted from the carbon tube with thin foot-tips that besides the leg inertia, also reduces the possibility of inadvertent collisions of the leg with the environment. In the proposed leg design, only two cables are passing the joints that improve the reliability of the design by reducing the chance of wear, entangling, or adverse cutting of the cables.

Regarding the connection of the servomotors, the prototype of the robot has been built using the Dynamixel AX-12A servomotors connected using a single daisy chain, with individual wire chain connecting each leg from the central hub. The robot torso and leg parts are 3D printed using Polylactic acid (PLA) material. Only the tibia part is attached to the servomotor using the off-the-shelf Bioloid frame for the Dynamixel AX-12A. The render of the robot CAD model is visualized in Fig. 2a, and the fully assembled robot is shown in Fig 1.

B. FORWARD KINEMATICS

The kinematic model of the HAntR is based on Denavit–Hartenberg (DH) convention. Five Cartesian coordinate systems cover the path from the body coordinate frame to the foot with four of them relative to the leg, as it is depicted in Fig. 3. Further, we introduce the global reference frame and express all the FKT and IKT results in this frame, which significantly simplifies the formulation of the locomotion control approach presented in Section IV. Notice that the global reference frame has its z-axis oriented in the negative direction of the normalized vector of gravitational

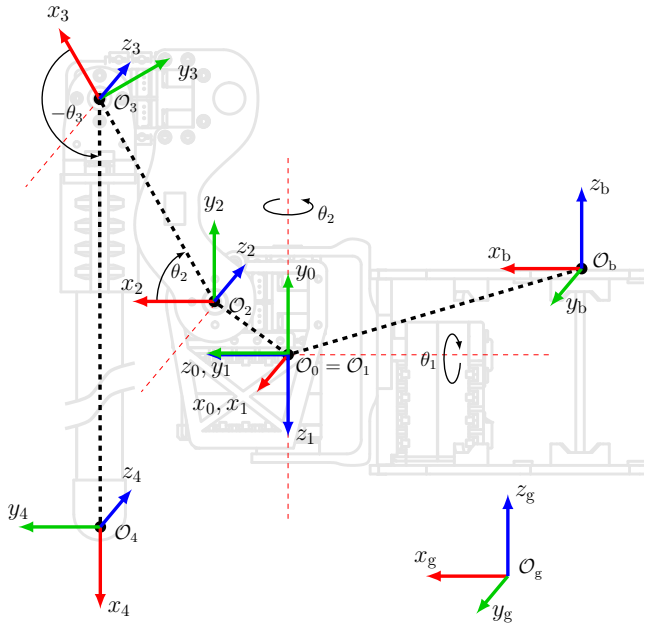

FIGURE 3. Structure of the HAntR leg.

acceleration ${}^{g}\mathbf{g}$. The FKT is as follows.

Let ${}^{g}\mathbf{p}$ be the foot-tip position of the leg in the global coordinate system and ${}^{4}\mathbf{p}$ be the foot-tip position in the foot-tip coordinate system. Then, the mapping between the global coordinate system and the foot-tip coordinate system is given by the kinematic chain

$$\begin{bmatrix} {}^{g}\mathbf{p} \\ 1 \end{bmatrix} = \mathbf{T}^{g}\,\mathbf{T}^{l}\,\mathbf{M}_1^0\,\mathbf{M}_2^1\,\mathbf{M}_3^2\,\mathbf{M}_4^3 \begin{bmatrix} {}^{4}\mathbf{p} \\ 1 \end{bmatrix}, \tag{1}$$

where $\mathbf{T}^{g}$ is the rigid body transformation representing the position and orientation of the robot body in the global reference frame, $\mathbf{T}^{l}$ is the rigid body transformation between the body coordinate frame and the coxa coordinate frame of the l-th leg, and $\mathbf{M}_{i+1}^{i}$ is the DH transformation matrix between adjacent leg coordinate systems given as

$$\mathbf{M}_i^{i-1} = \begin{bmatrix} c_{\psi_i} & -s_{\psi_i}\,c_{\alpha_i} & s_{\psi_i}\,s_{\alpha_i} & a_i\,c_{\psi_i} \\ s_{\psi_i} & c_{\psi_i}\,c_{\alpha_i} & -c_{\psi_i}\,s_{\alpha_i} & a_i\,s_{\psi_i} \\ 0 & s_{\alpha_i} & c_{\alpha_i} & d_i \\ 0 & 0 & 0 & 1 \end{bmatrix}, \tag{2}$$

$$\psi_i = \theta_i + \theta_i^{\text{off}},$$

where c_{ψ_i} and s_{ψ_i} denote $\cos(\psi_i)$ and $\sin(\psi_i)$, respectively, and $\alpha, a, \theta, \theta^{\text{off}}, d$ are the DH parameters with the particular values listed in Table 2.

Since the robot body is symmetric, the $\mathbf{T}^{l}$ transformation depends only on the mount angle of the l-th leg $\beta^{l} \in \{0, \frac{\pi}{3}, \frac{2\pi}{3}, \pi, \frac{4\pi}{3}, \frac{5\pi}{3}\}$, the radius of the body $l_r = 102\,\text{mm}$, and the vertical offset of the body center

TABLE 2. Values of the Denavit–Hartenberg Parameters

Link	i	α_i [rad]	a_i [mm]	d_i [mm]	θ_i^{off} [rad]	θ_i [rad]
Coxa	1	$\pi/2$	0	0	0	θ_1^l
Trochanter	2	-$\pi/2$	25.4	-18.5	$\pi/2$	θ_3^l
Femur	3	0	81.6	0	-0.52	θ_3^l
Tibia	4	0	205.5	0	-1.06	θ_4^l

$l_z = 38.5\,\text{mm}$ according to

$$\mathbf{T}^{l} = \begin{bmatrix} -s_{\beta^l} & 0 & c_{\beta^l} & l_r c_{\beta^l} \\ c_{\beta^l} & 0 & s_{\beta^l} & l_r s_{\beta^l} \\ 0 & 1 & 0 & l_z \\ 0 & 0 & 0 & 1 \end{bmatrix}. \tag{3}$$

C. INVERSE KINEMATICS

The IKT is to find the configuration of the joint angles $\boldsymbol{\theta}^{l} = \{\theta_1^l, \theta_2^l, \theta_3^l, \theta_4^l\}$ given the desired foot-tip coordinates ${}^{g}\mathbf{p} = [{}^{g}p_1, {}^{g}p_2, {}^{g}p_3]^T$ in the global reference frame, which solution is underdetermined because of the 4-DoF per leg. Although it is possible to reformulate the IKT by fixing the coxa joint angle θ_1^l or trochanter joint angle θ_2^l as in [42], instead we utilize the ideal foot-tip orientation vector ${}^{g}\mathbf{o} = [{}^{g}o_1, {}^{g}o_2, {}^{g}o_3]^T$ similarly to [25]. It imposes a constraint on the inverse kinematics solution such that the joint angles are calculated in the way to reach the given foot-tip coordinate ${}^{g}\mathbf{p}$ while minimizing the spatial angle between the tibia coordinate frame x-axis and the ideal foot-tip orientation vector ${}^{g}\mathbf{o}$ as it is visualized in Fig. 4.

Then, the solution of the IKT can be decomposed into finding the joint angles θ_1^l, θ_2^l that align the plane given by the leg base coordinate frame origin ${}^{g}\mathcal{O}_0^l$, desired foot-tip coordinate ${}^{g}\mathbf{p}$, and the ideal orientation vector ${}^{g}\mathbf{o}$ with the plane given by the femur and tibia links. Subsequently, we can find the planar solution for the joint angles θ_3^l, θ_4^l. The detailed description of the solution follows.

First, ${}^{g}\mathbf{p}$ and ${}^{g}\mathbf{o}$ are transformed into the leg-base coordinate frame using the inverse of the transformation $\mathbf{T}^{g}\mathbf{T}^{l}$. ${}^{g}\mathbf{o}$ is the orientation vector, and therefore, we transform only its rotation w.r.t. the coxa coordinate frame.

$$\begin{bmatrix} {}^{0}\mathbf{p} \\ 1 \end{bmatrix} = \left(\mathbf{T}^{g}\mathbf{T}^{l}\right)^{-1} \begin{bmatrix} {}^{g}\mathbf{p} \\ 1 \end{bmatrix}, \tag{4}$$

$${}^{0}\mathbf{o} = \begin{bmatrix} 1 & 0 & 0 & 0 \\ 0 & 1 & 0 & 0 \\ 0 & 0 & 1 & 0 \end{bmatrix} \left(\mathbf{T}^{g}\mathbf{T}^{l}\right)^{-1} \begin{bmatrix} 1 & 0 & 0 \\ 0 & 1 & 0 \\ 0 & 0 & 1 \\ 0 & 0 & 0 \end{bmatrix} {}^{g}\mathbf{o}. \tag{5}$$

Next, we denote the plane given by ${}^{0}\mathbf{p}$ and ${}^{0}\mathbf{o}$ as ρ_{FT} and calculate the normal vector ${}^{0}\mathbf{n}_{\rho} = \left({}^{0}n_{\rho_x}, {}^{0}n_{\rho_y}, {}^{0}n_{\rho_z}\right)$ to the plane as the cross product

$${}^{0}\mathbf{n}_{\rho} = {}^{0}\mathbf{o} \times {}^{0}\mathbf{p}. \tag{6}$$

There is a singular solution if $\|\mathbf{n}_{\rho}\| = 0$. In such a case, the joint angles are set as $\theta_1^l = \theta_2^l = 0$. Otherwise, the joint

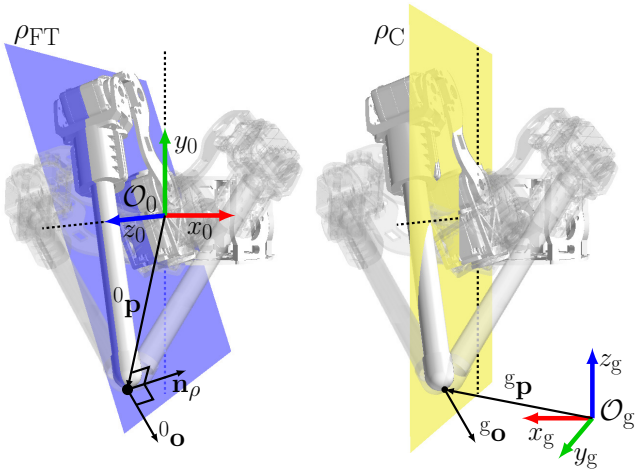

FIGURE 4. Visualization of possible solutions of the inverse kinematics task and the selected solution that minimizes the spatial angle between the tibia x-axis and the ideal foot-tip orientation vector ${}^{\mathrm{g}}\mathbf{o}$. A visualization of the femur-tibia plane with the construction of its normal vector ${}^0\mathbf{n}_\rho$ is on the left and the same situation with respect to the global reference frame is on the right.

angles θ_1^l, θ_2^l are given as the angles to align the plane ρ_{FT} and the plane ρ_{C} given as the yz-plane of the coxa coordinate system as it is shown in Fig. 4. The solution for the coxa joint angle θ_1^l and trochanter joint angle θ_2^l can be expressed as

$$\theta_1^l = \arctan\left(\frac{{}^0n_{\rho_y}}{{}^0n_{\rho_x}}\right), \tag{7}$$

$$\theta_2^l = \arcsin\left({}^0n_{\rho_z}\right). \tag{8}$$

Equations (7) and (8) represent the primary solution for the coxa and trochanter joints for configurations with the ideal orientation component ${}^{\mathrm{g}}o_z$ negative, thus, suitable for regular locomotion. Besides, there is an alternative solution $\hat{\theta}_1^l = \theta_1^l + \pi$, $\hat{\theta}_2^l = -\theta_2^l$ that we discard at this point, but can be considered, e.g., for object manipulation tasks.

After that, we can calculate ${}^2\mathbf{p}$ foot-tip position with respect to the femur joint using

$$\begin{bmatrix} {}^2\mathbf{p} \\ 1 \end{bmatrix} = \mathbf{A}^{l^{-1}} \begin{bmatrix} {}^{\mathrm{g}}\mathbf{p} \\ 1 \end{bmatrix}, \tag{9}$$

where $\mathbf{A}^l$ is the transformation matrix between the global coordinate frame and the femur coordinate frame calculated as the partial forward kinematics

$$\mathbf{A}^l = \mathbf{T}^{\mathrm{g}}\mathbf{T}^l\mathbf{M}_1^0\mathbf{M}_2^1. \tag{10}$$

The respective femur angle θ_3^l and tibia angle θ_4^l are then given according to the cosine law and the angle above the horizon

$$\theta_3^l = \arccos\left(\frac{a_3^2 - a_4^2 + \left\|{}^2\mathbf{p}\right\|^2}{2a_3\left\|{}^2\mathbf{p}\right\|}\right) - \arctan\left(\frac{{}^2p_2}{{}^2p_1}\right) - \theta_3^{\mathrm{off}}, \tag{11}$$

$$\theta_4^l = -\pi + \arccos\left(\frac{a_3^2 + a_4^2 - \left\|{}^2\mathbf{p}\right\|^2}{2a_3a_4}\right) - \theta_4^{\mathrm{off}}. \tag{12}$$

Note that a solution with the angle value above the horizon is used as the default solution, while a complementary solution with the angle below the horizon [56] exists, which further extends the kinematic capabilities of the robot. The detailed analysis of the leg workspace is presented in Section V-A. Here, it is further worth noting that by setting $\mathbf{T}^{\mathrm{g}} = \mathbf{I}$ in both the FKT and IKT, a traditional formulation for kinematics with four degrees of freedom is obtained. However, by introducing the global reference frame, we simplify the formulation of the control strategy design that is detailed in the following section.

IV. CONTROL DESIGN

The proposed morphology with the roll-yaw-pitch-pitch configuration of the leg extends the robot motion capabilities in comparison to the previous PhantomX AX robot. Therefore, a novel controller has been developed to exploit the robot capabilities and improve the overall performance of HAntR. The control architecture of HAntR and the robot terrain-sensing abilities are based on the adaptive locomotion approach [23]. Unlike [23], which divides the robot locomotion into the individual motion of the legs to new footholds followed by the body motion, we have modified the locomotion control to allow continuous body motion by exploiting the formulation of the FKT and IKT using the global reference frame. Further, an inclination controller is developed to exploit the leg's fourth degree of freedom and improve the robot locomotion capabilities when walking on steep inclines, contour lines, and in rough terrains.

During the locomotion, each leg alternates between the stance phase, when it is supporting the body, and the swing phase, when it is reaching a new foothold. The order in which legs alternate between the stance and swing phases is defined by the fixed-sequence locomotion gait that can be described as a sequence $\mathcal{G}$ of the sets of concurrently swinging leg. Hence, $\mathcal{G}$ is given as $\mathcal{G} = \{\mathcal{G}_i \,|\, i \in \{1, \cdots, n_{\mathrm{gp}}\}\}$, where $\mathcal{G}_i$ is the set of leg IDs used within a single gait phase i and n_{gp} is the overall number of gait phases. The utilized locomotion gaits are: the tripod gait $\mathcal{G} = \{\{1,3,5\},\{2,4,6\}\}$; tetrapod gait $\mathcal{G} = \{\{1,5\},\{2,4\},\{3,6\}\}$; and pentapod gait $\mathcal{G} = \{\{1\},\{6\},\{2\},\{5\},\{3\},\{4\}\}$ with the particular number of the gait phases $n_{\mathrm{gp}} = 2$, $n_{\mathrm{gp}} = 3$, and $n_{\mathrm{gp}} = 6$, respectively. Besides, the formulation of the controller can be easily modified to support free-sequence gaits or kinematic-margin based approaches [57] for selection of swinging legs, which is, however, out of the scope of this paper.

The robot locomotion is controlled in the complete gait cycles with n_{gp} individual phases and the desired gait cycle execution time t_{g}. During each gait cycle, all the legs transfer from their original configurations to new configurations within the time t_{g}, while the body pose is continuously optimized to cope with the terrain irregularities and current terrain inclination. The internal control loop is synchronized with the hardware control period of $T_{\mathrm{con}} = 25\,\mathrm{ms}$ that is given by the achievable communication speed of the employed servomotors [58]. The control period T_{con} is deter-

TABLE 3. Used Symbols

Symbol	Description
Gait-related symbols	
$\mathcal{G}$	Fixed-sequence gait prescribed as a sequence of sets of concurrently swinging leg IDs $\mathcal{G} = \{\mathcal{G}_i \mid i \in \{1, \cdots, n_{\text{gp}}\}\}$.
$\mathcal{G}_i$	Set of the leg IDs in the gait phase i.
n_{gp}	Number of gait phases $n_{\text{gp}} = \|\mathcal{G}\|$.
$\mathcal{G}_{\text{swing}}$	Set of the currently swinging leg IDs $\mathcal{G}_{\text{swing}} \subseteq \mathcal{G}_i$.
Timing-related symbols	
t_{g}	Desired gait cycle execution time, i.e., the desired time for transferring all legs from the current footholds to the new desired footholds.
T_{con}	Control-cycle period.
Control inputs symbols	
v_x	Control command: forward speed $[\text{m}\,\text{s}^{-1}]$.
v_y	Control command: sideways speed $[\text{m}\,\text{s}^{-1}]$.
ω_z	Control command: angular speed $[\text{rad}\,\text{s}^{-1}]$.
${}^{\text{g}}\mathbf{g}$	Normalized gravitational vector in the global coordinate frame.
Kinematics-related symbols	
l	Leg ID $l \in \{1 \cdots 6\}$
$\mathbf{T}^{\text{g}}$	Body pose represented as rigid transformation matrix in the global coordinate frame.
$\mathcal{P}_{\text{def}}$	Set of the default footholds in the global coordinate frame $\mathcal{P}_{\text{def}} = \{{}^{\text{g}}\mathbf{p}^l_{\text{def}} \mid l \in \{1, \cdots, 6\}\}$.
$\mathcal{P}_{\text{curr}}$	Set of the current footholds in the global coordinate frame $\mathcal{P}_{\text{curr}} = \{{}^{\text{g}}\mathbf{p}^l_{\text{curr}} \mid l \in \{1, \cdots, 6\}\}$.
$\mathcal{P}_{\text{new}}$	Set of new desired footholds in the global coordinate frame $\mathcal{P}_{\text{new}} = \{{}^{\text{g}}\mathbf{p}^l_{\text{new}} \mid l \in \{1, \cdots, 6\}\}$.
$\mathcal{P}$	Set of immediate foot-tip poses in the global coordinate frame $\mathcal{P} = \{{}^{\text{g}}\mathbf{p}^l \mid l \in \{1, \cdots, 6\}\}$.
$\boldsymbol{\theta}^l_{\text{des}}$	The desired joint angles of the leg l.
$\boldsymbol{\theta}^l_{\text{real}}$	The sampled joint angles of the leg l.

mined in accordance with the foot-contact detection mechanism that requires writing a new desired position and reading the current position of all the servos within the control period. The whole control algorithm is summarized in Algorithm 1 and schematically visualized in Fig. 5. For better orientation in Algorithm 1, Fig. 5, and the following detailed description of the control strategy, a list of used symbols with description is provided in Table 3. A detailed description of the control strategy follows.

First, the current pose $\mathcal{P}_{\text{curr}} = \{{}^{\text{g}}\mathbf{p}^l_{\text{curr}} \mid l \in \{1, \cdots, 6\}\}$ of the legs is sampled by reading out all the robot joint angle positions $\boldsymbol{\theta}_{\text{real}}$ and calculating the pose using the forward kinematics.[1]

A new set of desired foothold coordinates $\mathcal{P}_{\text{new}} = \{{}^{\text{g}}\mathbf{p}^l_{\text{new}} \mid l \in \{1, \cdots, 6\}\}$ given in the global reference frame are calculated based on the current body pose and the default set of the robot footholds that are parameterized by the default leg span $d_{\text{def}} = 240\,\text{mm}$ and the default body ground clearance $h_{\text{def}} = 100\,\text{mm}$, the high-level steering command (v_x, v_y, ω_z) of the forward speed, sideways speed, and the angular speed, respectively, and also according to the desired

[1]Notice that during the continuous locomotion, $\boldsymbol{\theta}_{\text{real}}$ joint angle values from the previous gait cycle are used instead of fetching new values as the joint angle readout is the most time-consuming operation that takes 24 ms.

Algorithm 1: Gait cycle execution

Input: $\mathcal{G}$ – the fixed-sequence gait prescribed as a sequence of sets of concurrently swinging leg IDs
Input: n_{gp} – the number of gait phases
Input: t_{g} – gait cycle execution time
Input: v_x, v_y, ω_z – gait cycle parametrization

```
θ_real ← ReadAllServoPositions()
P_curr ← CalcCurrentFootholds(θ_real)
P_new ← CalcNewFootholds(v_x, v_y, ω_z)
n_sp ← t_g/(n_gp T_con)        // no. of leg swing poses
for each gait phase i ∈ {1, ..., n_gp} do
    G_swing ← G_i              // select swinging legs
    k ← 0                      // reset execution counter
    while not G_swing empty do // control loop
        for each leg l ∈ {1, ..., 6} do
            if l ∈ G_swing then
                gp^l ← CalcNextPose(gp^l_curr, gp^l_new, n_sp, k)
                                // next swing pose
            else
                gp^l ← gp^l    // hold pose
        gg ← SampleIMU()
        T^g ← CalcBodyPose(gp, gg)
        go ← gg
        for each leg l ∈ {1, ..., 6} do
            θ^l_des ← CalcLegIKT(l, T^g, gp^l, go)
        SetAllServoPositions(θ_des)
        θ_real ← ReadAllServoPositions()
        for each leg l ∈ G_swing do
            if TactileSensing(θ^l_des, θ^l_real) = 1 then
                G_swing ← G_swing \ l   // stop the l-th leg
        k ← k + 1
```

gait cycle execution time t_{g} for each leg $l \in \{1, \cdots, 6\}$. The new desired footholds coordinates can be expressed as

$$\begin{bmatrix} {}^{\text{g}}\mathbf{p}^l_{\text{new}} \\ 1 \end{bmatrix} = \begin{bmatrix} c_{\omega_z t_g} & -s_{\omega_z t_g} & 0 & v_x t_g \\ s_{\omega_z t_g} & c_{\omega_z t_g} & 0 & v_y t_g \\ 0 & 0 & 1 & 0 \\ 0 & 0 & 0 & 1 \end{bmatrix} \begin{bmatrix} {}^{\text{g}}\mathbf{p}^l_{\text{def}} \\ 1 \end{bmatrix}, \quad (13)$$

where ${}^{\text{g}}\mathbf{p}^l_{\text{def}} = \left[d_{\text{def}}\, s_{\beta^l}, d_{\text{def}}\, c_{\beta^l}, -h_{\text{def}}\right]^T$ is the leg default foothold.

Once new footholds are determined, the legs swing from their current poses to new foothold poses according to the prescribed gait. The main control loop consists of phases of deciding the immediate foot-tip pose ${}^{\text{g}}\mathbf{p}^l$ of each leg in the global reference frame followed by the optimization of the body pose $\mathbf{T}^{\text{g}}$ using the sampled vector of gravity

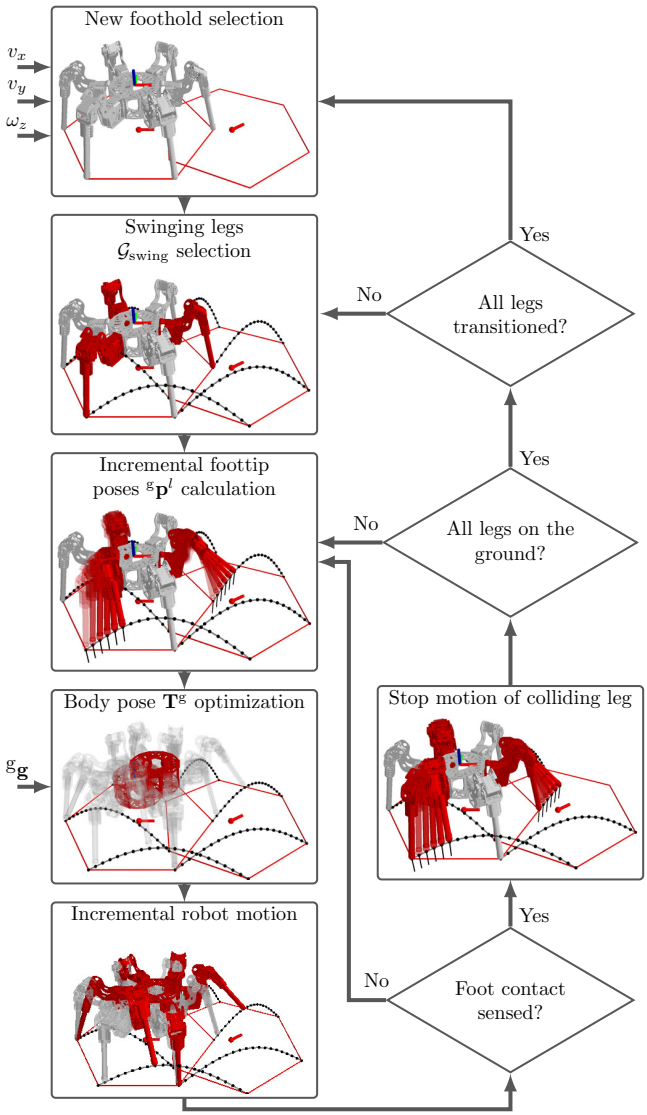

FIGURE 5. Overview of the proposed control architecture for the HAntR.

${}^{\text{g}}\mathbf{g}$. Then, the joint angles $\boldsymbol{\theta}^l_{\text{des}}$ for each leg are calculated using the inverse kinematics, and position controllers of the servomotors are set accordingly.

Finally, the current pose of the legs is sampled by reading out all the robot joint angle positions $\boldsymbol{\theta}_{\text{real}}$ that is compared to the desired joint angles $\boldsymbol{\theta}^l_{\text{des}}$ for detection of foot-contact events according to the scheme presented in [23] and further detailed in Section IV-A. The execution of the gait cycle ends when all the legs have swung, and they have ground contact.

The immediate foot-tip poses ${}^{\text{g}}\mathbf{p}^l$ are selected either to hold the current pose in the global reference frame, when the respective leg is in the stance phase, or as one of the intermittent points on the path between the leg current foothold ${}^{\text{g}}\mathbf{p}^l_{\text{curr}}$ and the new desired foothold ${}^{\text{g}}\mathbf{p}^l_{\text{new}}$. The leg is supposed to reach the new foothold within the time $t_{\text{sp}} = t_{\text{g}}/n_{\text{gp}}$. Hence, given the control cycle period T_{con} there are $n_{\text{sp}} = t_{\text{g}}\ n_{\text{gp}}^{-1}\ T_{\text{con}}^{-1}$ individual poses on the path between ${}^{\text{g}}\mathbf{p}^l_{\text{curr}}$ and ${}^{\text{g}}\mathbf{p}^l_{\text{new}}$. We have selected the positive amplitude of the sine wave as the desired leg path for its smooth profile, although more elaborated swing path can be designed considering the leg dynamics and terrain characteristics, e.g., as in [25], [52], [59]; however, such a trajectory optimization requires exteroceptive sensing and is out of the scope of the presented design of the HAntR. Hence, the immediate foot-tip pose ${}^{\text{g}}\mathbf{p}^l$ at the control cycle k is computed as

$$ {}^{\text{g}}\mathbf{p}^l = {}^{\text{g}}\mathbf{p}^l_{\text{curr}} + \frac{k}{n_{\text{path}}} \left(\Delta\mathbf{p}^l + \begin{bmatrix} 0 \\ 0 \\ h_{\text{st}} \sin\left(k \frac{\pi}{n_{\text{path}}} \right) \end{bmatrix} \right), \tag{14} $$

$$ \Delta\mathbf{p}^l = {}^{\text{g}}\mathbf{p}^l_{\text{new}} - {}^{\text{g}}\mathbf{p}^l_{\text{curr}}, \tag{15} $$

where h_{st} is the pre-defined height of the leg step. The leg foot-tip path is prescribed in the global reference frame, and thus the body-pose can be altered without affecting the leg transition in the global reference frame.

The body pose optimization is to provide the robot body with a smooth motion and distribute its weight evenly among the individual legs and thus reduces the joint torques. The body pose is prescribed by the rigid body transformation $\mathbf{T}^{\text{g}}$ that consists of the translational part $\mathbf{T}^{\text{g}}_{\text{tran}}$ and rotational part $\mathbf{T}^{\text{g}}_{\text{rot}}$. Using the formulation of kinematics and controller in the global reference frame, the computation of the translational part reduces into the calculation of the centroid of the leg foot-tips followed by the projection of the center of mass in the opposite direction to the normalized gravitational vector ${}^{\text{g}}\mathbf{g}$ as

$$ \mathbf{T}^{\text{g}}_{\text{tran}} = \frac{1}{6} \sum_{l=1}^{6} {}^{\text{g}}\mathbf{p}^l - h_{\text{def}} \frac{{}^{\text{g}}\mathbf{g}}{\|{}^{\text{g}}\mathbf{g}\|}. \tag{16} $$

The rotational part is then assigned as the rotation around the z-axis by the mean angle between the legs default poses ${}^{\text{g}}\mathbf{p}_{\text{def}}$ and the current poses ${}^{\text{g}}\mathbf{p}$

$$ \varphi = \frac{1}{6} \sum_{l=1}^{6} \operatorname{atan} \left(\frac{\left\| {}^{\text{g}}\mathbf{p}^l_{\text{def}} \times \left({}^{\text{g}}\mathbf{p}^l - \mathbf{T}^{\text{g}}_{\text{tran}} \right) \right\|}{{}^{\text{g}}\mathbf{p}^l_{\text{def}} \cdot \left({}^{\text{g}}\mathbf{p}^l - \mathbf{T}^{\text{g}}_{\text{tran}} \right)} \right), \tag{17} $$

$$ \mathbf{T}^{\text{g}}_{\text{rot}} = \begin{bmatrix} c_\varphi & -s_\varphi & 0 \\ s_\varphi & c_\varphi & 0 \\ 0 & 0 & 1 \end{bmatrix}. \tag{18} $$

The body-pose always follows the legs such that the mass is distributed evenly among them during the stance phase. The straight-forward selection of the ideal foot-tip orientation vector in the direction of the normalized gravitational vector ${}^{\text{g}}\mathbf{o} = {}^{\text{g}}\mathbf{g}$ is suggested in [25], [42] and it ensures balanced distribution of the weight between individual legs. Based on the set of the current poses ${}^{\text{g}}\mathbf{p}$, the ideal orientation vector ${}^{\text{g}}\mathbf{o}$, and the body-pose $\mathbf{T}^{\text{g}}$, the joint angles $\boldsymbol{\theta}_{\text{des}}$ for all legs are calculated using the inverse kinematics as it is described in Section III-C.

The body-pose always follows the legs such that the mass is distributed evenly among them during the stance phase,

and the body movement has a smooth velocity profile without abrupt accelerations and decelerations. The body velocity profile is presented in Section V-C and compared to the original adaptive locomotion approach with the discretized body motion [23].

A. FOOT-CONTACT DETECTION

The ability to sense the contact between the robot foot and the ground and obstacles is essential for all legged robots to react to terrain irregularities and to overcome rough terrains. For the terrain sensing, we follow the approach described in [23] that utilizes only the position feedback of the servomotors for foot-contact sensing. In particular, the approach is based on a comparison of the currently set joint positions $\boldsymbol{\theta}_{\text{des}}$ and the actual real-world joint positions $\boldsymbol{\theta}_{\text{real}}$ with the error threshold $\mathbf{e}_{\text{thld}}$ calculated using the inverse dynamics model of the leg. The approach [23] formulates the inverse dynamics task and estimation of $\mathbf{e}_{\text{thld}}$ for two degrees of freedom only in case the leg follows a rectangular trajectory with fixed coxa joint during the swing-down phase. Based on the experimental evaluation, we experienced that for HAntR, a fixed threshold value is sufficient for terrain sensing because of the lightweight femur and tibia parts of the leg that positively influences the leg inertia. Hence, the foot-contact sensing is realized as a simple comparison

$$\|\theta^i_{\text{des}} - \theta^i_{\text{real}}\| < e^i_{\text{thld}}, \tag{19}$$

for the experimentally found threshold values of $\mathbf{e}^1_{\text{thld}} = \mathbf{e}^2_{\text{thld}} = 0.05\,\text{rad}$ and $\mathbf{e}^3_{\text{thld}} = \mathbf{e}^4_{\text{thld}} = 0.09\,\text{rad}$ for the coxa ($i = 1$), trochanter ($i = 2$), femur ($i = 3$), and tibia ($i = 4$) joints, respectively.

Although a further extension of the dynamic model used in [23] is possible also for the herein presented 4-DoF leg design, we dedicate it for future work, as HAntR demonstrated significantly improved locomotion capabilities and sufficient reliability in comparison to the previous platform utilized in [23]. Besides, the presented control approach improves the robot weight distribution between individual legs, which is especially beneficial during locomotion in sloped terrains. Further, the adaptive terrain sensing does not require any additional sensors for the robot to overcome rough terrains. Besides, the representation of the kinematics tasks in the global reference frame greatly simplifies the formulation of the control approach, which, in turn, is easily extendable to full deliberative control that requires exteroceptive sensing [44], [60]. The performance of the presented locomotion controller in the real-world deployment of the built prototype of HAntR is reported in the next section.

V. EXPERIMENTAL EVALUATION

The proposed design and locomotion control strategy have been verified with the prototype HAntR in a series of deployments to evaluate its characteristics. First, we present an analysis of the leg workspace to show the enhanced kinematic capabilities of the proposed leg design with a compact body. Then, results on the real-world experimental deployments are reported to demonstrate achieved locomotion capabilities in rough terrains, including dynamic and static adaptation to locomotion on sloped surfaces. Finally, since our motivation for the development of HAntR has been to improve not only locomotion capabilities in rough and unstructured terrains but also to increase locomotion speed and endurance, we report on experimental comparison of the newly designed robot with its predecessor PhantomX AX robot [39] with the same servomotors Dynamixel AX-12A.

All the experiments have been performed with the same hardware setup. In particular, the robot central controller platform is the Odroid XU-4 with 2 GHz ARM Cortex A7 octa-core processor (Samsung Exynos5422) with 2 GB RAM running Ubuntu 18.04 and ROS-melodic. In addition to the position feedback of the servomotors, the attitude and heading reference system (AHRS) Xsense MTi-30 unit, with $400\,\text{Hz}$ sampling rate, has been utilized as the input to the locomotion controller. The OptiTrack motion capture system has provided the robot 6-DoF pose reference in the slope adaptation experiment with $30\,\text{Hz}$ localization rate, and the robotic total station Leica TS-16 has been used for 3-DoF pose reference during the locomotion tests on rough terrain with $10\,\text{Hz}$ localization rate.

The HAntR performance in the experimental evaluation is shown in the accompanying video from the real deployment[2].

A. ANALYSIS OF THE LEG WORKSPACE

The leg workspace analysis is supposed to verify the enhanced motion capabilities of HAntR enabled by the fourth DoF of the proposed morphology. The fourth DoF extends the possible range of the leg, and for most of the reachable positions, it also allows multiple configurations of the leg, which can be observed in Fig. 4.

We have used the reverse projection of the sampled joint angles $\boldsymbol{\theta}$ to evaluate the shape of the leg workspace and to verify the implementation of the inverse kinematics module. First, joint angles are sampled according to Table 4 that render altogether $1\,749\,600$ different workspace configurations $\boldsymbol{\theta}$ in the four dimensional mesh grid of the leg workspace.

TABLE 4. Leg workspace evaluation parameters

Link	i	$\theta_i^{\min}$ [rad]	θ_i^{max} [rad]	$\Delta\theta_i$ [rad]
Coxa	1	$-\pi/2$	$\pi/2$	$\pi/30$
Trochanter	2	$-3\pi/5$	$3\pi/5$	$\pi/30$
Femur	3	$-\pi/2$	π	$\pi/30$
Tibia	4	$-3\pi/5$	$3\pi/5$	$\pi/30$

The configurations are then projected using the forward kinematics and checked for collisions. The Robust and Accurate Polygon Interference Detection (RAPID) library [61] has been used for collision checking between the individual leg parts and the robot body. If the sampled configuration

[2]https://youtu.be/DFOFj2T4b5s.

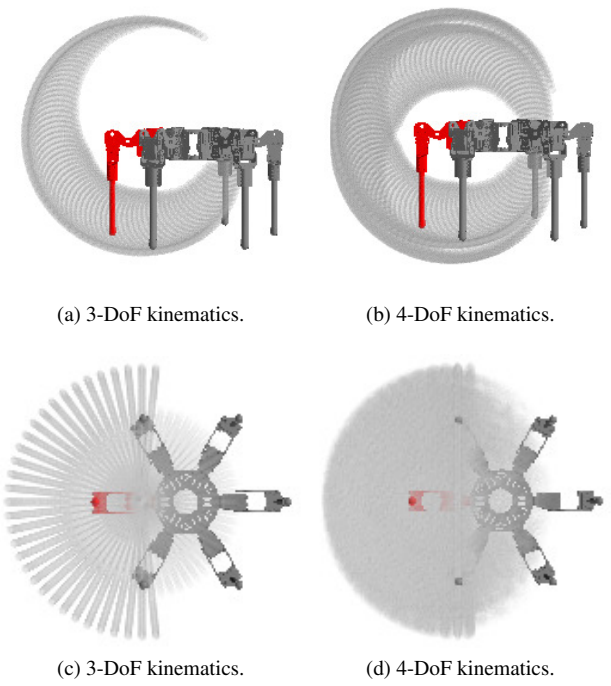

(a) 3-DoF kinematics. (b) 4-DoF kinematics.

(c) 3-DoF kinematics. (d) 4-DoF kinematics.

FIGURE 6. Visualization of the leg workspace. (a) Frontal plane cut of configurations reachable using 3-DoF kinematics ($\theta_1 = 0$). (b) Frontal plane cut of configurations reachable using 4-DoF kinematics ($\theta_1 \in \{0, \pi\}$). (c) Transverse plane projection of leg workspace for 3-DoF kinematics. (d) Transverse plane projection of leg workspace for 4-DoF kinematics.

does not render the leg colliding, the world position ${}^{\mathrm{g}}\mathbf{p}$ is calculated together with the desired ideal orientation ${}^{\mathrm{g}}\mathbf{o}$ using the forward kinematics as the position of the coordinate system center ${}^{\mathrm{g}}\mathcal{O}_4$ and the vector given by ${}^{\mathrm{g}}\mathcal{O}_3$ and ${}^{\mathrm{g}}\mathcal{O}_4$, respectively. Finally, the solution of the IKT presented in Section III-C is applied for the obtained ${}^{\mathrm{g}}\mathbf{p}$ and ${}^{\mathrm{g}}\mathbf{o}$ to verify that the sampled and calculated joint angles $\boldsymbol{\theta}$ coincide. For all the sampled configurations, the IKT provides the correct result.

Fig. 6 shows the comparison of the leg workspace for 3-DoF and 4-DoF kinematics. Note, the 3-DoF configurations exclude coxa motion, hence $\theta_1 = 0$ for these configurations. In particular, Fig. 6a and Fig. 6b show the frontal plane cut of the leg workspace for 3-DoF and 4-DoF, respectively. It can be seen that the fourth DoF extends the possible range of motion and effectively allows the robot to flip over without spoiling its locomotion capabilities.

Fig. 6c and Fig. 6d show the transverse plane projection of all the reachable configurations given by the sampling described in Table 4, where each configuration is rendered as a point with 0.01 opacity in the figures. By comparing the reachable 3-DoF configurations visualized in Fig. 6c and 4-DoF configurations visualized in Fig. 6d, it can be seen a significant improvement in the amount of possible reachable non-colliding configurations.

B. FOOT-CONTACT SENSING EVALUATION

The feasibility of the utilized foot-contact detection method [23] is verified in this test. The experiment has been performed with the robot walking on the flat surface using the tripod gait parameterized by the gait cycle execution time $t_{\mathrm{g}} = 1\,\mathrm{s}$, with the leg $l = 1$ stepping on the $6\,\mathrm{cm}$ height obstacle. At the same time, we recorded the desired joint position θ_{des} set by the locomotion controller and the current real-world position of the robot joint θ_{real} given as the feedback of the robot servo motors during the leg swing phase.

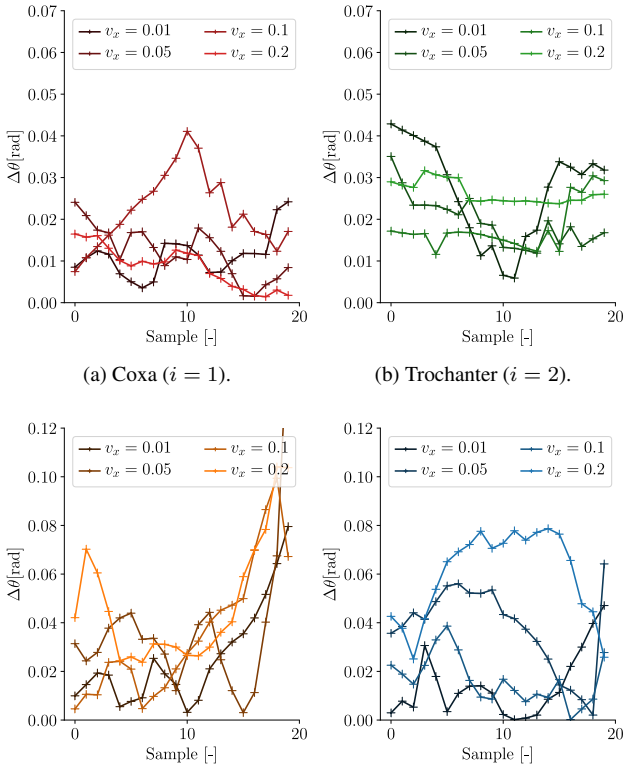

(a) Coxa ($i = 1$). (b) Trochanter ($i = 2$).

(c) Femur ($i = 3$). (d) Tibia ($i = 4$).

FIGURE 7. Joint error $\Delta\theta^i = \|\theta^i_{\mathrm{des}} - \theta^i_{\mathrm{real}}\|$ during the leg swing phase for different velocity.

Representative examples of joint errors $\Delta\theta^i = \theta^i_{\mathrm{des}} - \theta^i_{\mathrm{real}}$ for individual joints of the first leg $l = 1$ with different swing lengths complying to $v_x \in \{0.01, 0.05, 0.1, 0.2\}[\mathrm{m\,s^{-1}}]$ are shown in Fig. 7. The contact of the leg with the ground can be seen in the plots of the femur angle response as the rapid increase in the joint angle error. The rapid increase of the joint angle error $\Delta\theta^3$ over the fixed threshold $e^3_{\mathrm{thld}} = 0.09\,\mathrm{rad}$ results in the tactile event detection and subsequent stopping of the leg motion. It can be observed from the plots, that there are 20 joint position samples within the control period t_{con} for the given gait cycle execution time $t_{\mathrm{g}} = 1\,\mathrm{s}$ of the tripod gait. Furthermore, a rather flat profile of the individual joint error readings can be observed. It is caused by the lightweight construction of the leg for which the leg foot-tip accurately follows the given trajectory that simplifies the tactile sensing.

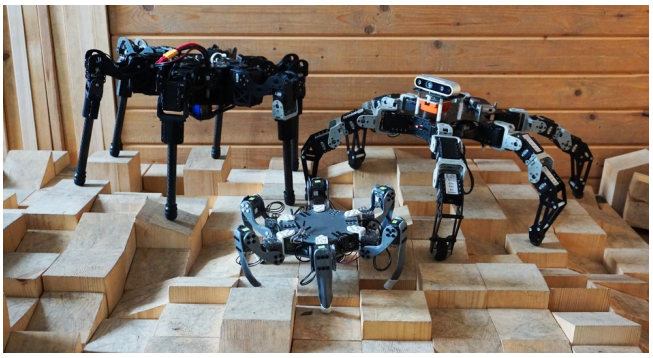

FIGURE 8. HAntR (left), PhantomX AX (right), and small hexapod walking robot with Dynamixel XL-320 servomotors (middle) on the rough terrain testbed.

C. ADAPTIVE LOCOMOTION IN ROUGH TERRAINS

Enhanced rough terrain locomotion is the essential motivation behind the development of the new robot. Therefore, an experimental benchmarking of the locomotion capabilities and motion effectiveness has been carried out to test the robot ability to overcome rough terrains and compare the HAntR with the PhantomX AX platform controlled using the original locomotion controller [23]. The experiment has been carried out in the laboratory environment on flat ground and a rough-terrain testbed. Both of the robots and the experimental testbed are shown in Fig. 8. The testbed of size $2.3\,\mathrm{m} \times 1.0\,\mathrm{m}$ is composed of squared $10\,\mathrm{cm} \times 10\,\mathrm{cm}$ wooden cubes with irregular height and slope, and with the maximum inter-block height difference of 9 cm.

During the experiment, the robot has been guided over the terrains in individual trials using different locomotion gait (tripod, tetrapod, pentapod). For HAntR, the individual locomotion gaits have been parameterized such that the gait cycle execution time t_g matches the ones of the PhantomX AX locomotion controller [23]. In particular, $t_\mathrm{g} = 1.2\,\mathrm{s}$ for the tripod gait, $t_\mathrm{g} = 1.8\,\mathrm{s}$ for the tetrapod gait, and $t_\mathrm{g} = 3.6\,\mathrm{s}$ for the pentapod gait.

The velocity and power consumption of the robot have been measured for individual trials to evaluate the effectiveness of the robot locomotion using the Cost of Transport (CoT) metric [59] estimated using the formula:

$$\mathrm{CoT} = \frac{\overline{P}}{m\,g\,\overline{v}}, \tag{20}$$

where $\overline{P}$ is the mean power consumption, m is the weight of the robot, $\overline{v}$ is the mean locomotion speed, and $g = 9.81\,\mathrm{m\,s^{-2}}$ is the gravitational acceleration.

In our experiments the mean power consumption has been calculated as the arithmetic mean of the instantaneous power consumption as:

$$\overline{P} \simeq \frac{1}{n_\mathrm{power}} \sum_{i=1}^{n_\mathrm{power}} \left(U_i^\mathrm{inst}\, I_i^\mathrm{inst} \right), \tag{21}$$

where U_i^inst and I_i^inst are the instantaneous voltage and current drawn from the battery at the sample step i. The instantaneous voltage and current have been sampled with $500\,\mathrm{Hz}$ sampling rate. The locomotion speed has been estimated from the localization data provided by the Leica TS-16 robotic total station with $10\,\mathrm{Hz}$ rate using the formula:

$$\overline{v} \simeq \frac{1}{n_\mathrm{loc}} \sum_{i=1}^{n_\mathrm{loc}} \frac{\Delta s_i}{\Delta t_i}, \tag{22}$$

where Δs is the distance difference between two consecutive localization samples and $\Delta t = 0.1\,\mathrm{s}$ is the time between the consecutive samples.

Each of the experimental trials has been performed ten times to evaluate the performance of the robot statistically. Five-number summary for each experimental trial is visualized in Fig. 9a and Fig. 9b for flat and rough terrains, respectively. The CoT results indicate the improved performance of HAntR in comparison to the PhantomX AX robot given the increased mass and six more actuators of HAntR. However, the reported results on the CoT are for the specific parametrization of the HAntR locomotion gait that is given by both the gait cycle execution time t_g and the desired velocity command of the robot. Therefore, we further experimentally tuned the gait cycle execution time t_g to achieve the maximum locomotion speed of HAntR about $0.428\,\mathrm{m\,s^{-1}}$ with the measured precision $\pm 0.022\,\mathrm{m\,s^{-1}}$, which corresponds to $87\,\%$ of the default robot size. The speed is achieved for the tripod gait and $t_\mathrm{g} = 0.32\,\mathrm{s}$ that for the prohibitively long control period $T_\mathrm{con} = 25\,\mathrm{ms}$ gives only six sampling points for tactile sensing during the swing phase of the leg. The achieved maximum speed is thus suitable for flat terrain locomotion only; however, using servomotors with faster communication or additional tactile sensing, it might be suitable also for rough terrain, which is a subject of the future work. Similarly, the maximum locomotion speed of HAntR for rough terrains is about $0.161\,\mathrm{m\,s^{-1}}$ with the measured precision $\pm 0.017\,\mathrm{m\,s^{-1}}$, which corresponds to $33\,\%$ of the default robot size.

A vital characteristic of the rough terrain locomotion is the stability of the platform and smoothness of its motion. Abrupt motions of the relatively heavy body of the robot may lead to loss of balance due to the legs slippage. The herein presented locomotion controller is specifically designed to ensure smooth body motion. Fig. 10 shows the body velocity profile comparison for HAntR and PhantomX AX when walking over the terrain testbed using the tripod gait with $0.05\,\mathrm{m\,s^{-1}}$ forward velocity and matching gait cycle execution time of $t_\mathrm{g} = 2.0\,\mathrm{s}$. The profile clearly shows the abrupt nature of the PhantomX AX controller [23], whereas the body motion of HAntR is smoother.

D. EVALUATION OF SLOPE ADAPTATION

The main expected benefit of the fourth DoF of the leg has been experimentally evaluated on the static and dynamic stability of the robot on an inclined surface. In the stability test, the robot is supposed to hold static and dynamic stability on an increasingly sloped desk with a high friction

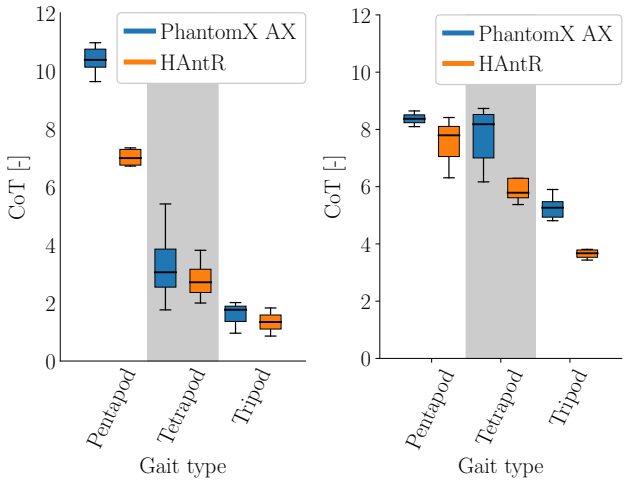

(a) Robot CoT on flat terrain. (b) Robot CoT on rough terrain.

FIGURE 9. Five-number summary of the robot Cost of Transport (CoT) with different gait parametrizations for (a) the flat terrain, (b) the rough terrain mock-up.

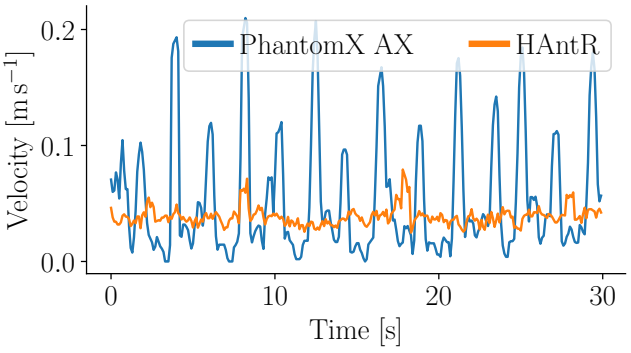

FIGURE 10. Comparison of the body velocity profile for HAntR driven by the herein proposed controller and PhantomX AX driven by the locomotion controller [23].

surface. The slope of the desk is monitored using the motion capture system, while the desired θ_{des} and real θ_{real} robot joint positions are collected for the evaluation. During the static stability test the robot holds its footholds while in the dynamic stability test the robot is treading at the place using the tripod gait.

Two sets of the experiments have been performed, with and without the inclination control, to assess the effect of the fourth DoF and the performance of the proposed controller. In the case the inclination controller is turned on, the vector of gravitational acceleration ${}^{\text{g}}\mathbf{g}$ is obtained by sampling the body-attached AHRS. For the disabled inclination controller, the gravitational vector is set to the fixed value of ${}^{\text{g}}\mathbf{g} = (0, 0, -1)^T$. The absolute foot-tip position error is used as the performance indicator, because HAntR does not feature force or torque sensors to measure the forces in individual legs directly. In the steady-state, the servomotor position error $\Delta\theta^i = \theta^i_{\text{des}} - \theta^i_{\text{real}}$ is proportional to the joint torque due to the servomotor P-type controller; hence, the chosen performance indicator is valid in such a case. The robot posture and the absolute foot-tip position error $d^l_{\text{err}} = \|\mathbf{p}^l_{\text{curr}} - \mathbf{p}^l_{\text{real}}\|$ are depicted in Fig. 11.

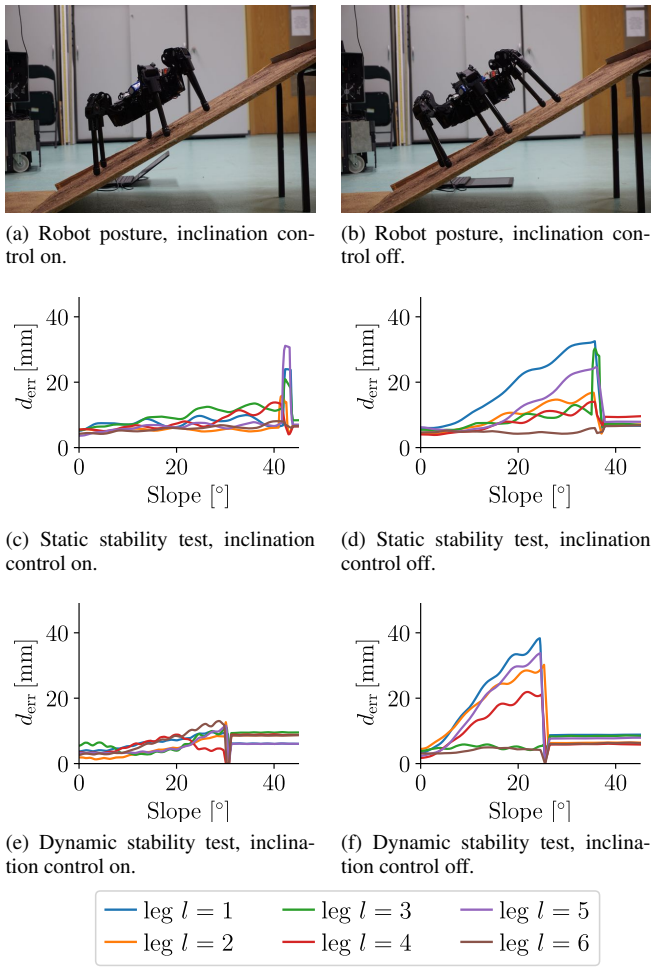

(a) Robot posture, inclination control on.
(b) Robot posture, inclination control off.
(c) Static stability test, inclination control on.
(d) Static stability test, inclination control off.
(e) Dynamic stability test, inclination control on.
(f) Dynamic stability test, inclination control off.

FIGURE 11. Snapshots of the robot and foot-tip position errors in slope adaptation experiment with the inclination control on (on the left) and off (on the right).

Based on the experimental evaluation, HAntR is able to walk on the surface with the slope up to 31°, and it remains statically stable up to 43° with the inclination control turned on. Without the inclination control, the stable walk has been observed for up to 26°, and the robot remains stable up to 37°, which supports the benefit of the additional DoF and employed locomotion control strategy. Although the inclination controller improves the absolute maximum ratings in the slope only slightly, a significant improvement in the weight distribution can be observed for the four DoF leg with the inclination control.

E. ROBOT ENDURANCE EVALUATION

In this test, we experimentally benchmark the robot endurance and its capacity to carry additional payload. Two critical factors are influencing the robot endurance, the battery life and overheating of the servomotors that may damage

the actuators and make the robot inoperative. The endurance benchmark has been thus performed in an air-conditioned environment with a fixed temperature of 23 °C. The robot has been equipped with a single fully charged 11.1 V Li-Poly battery of 2600 mA h capacity with the weight of 198.5 g. Before the trial run, the robot has been left standing in the default position which makes the servomotors to reach approximately 37 °C. After the warming up (or cool down after the first trial), the robot has been manually guided to wander around the building corridors using the tripod gait with $t_g = 1$ s and the limited speed $v_x = 0.18\,\mathrm{m\,s^{-1}}$.

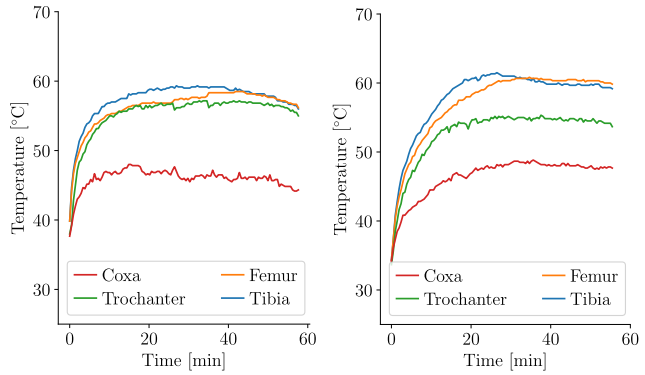

(a) Without additional payload. (b) Additional payload.

(c) Robot carrying 2460 g of additional payload.

FIGURE 12. Evolution of the mean temperature of the robot servomotors during the endurance experiment and the robot carrying the additional payload.

In three consecutive trials, the recorded robot endurance was 63, 68, and 62 minutes of the continuous locomotion with the traversed distance around 370 m, 400 m, and 420 m, respectively. A representative evolution of the servomotors temperature during the third experiment is visualized in Fig. 12a.

Next, we performed another three trials with an additional payload of 3× of the battery pack with the weight of 820 g that is 2460 g in the total and equals about 85 % of the robot nominal weight. The robot carrying the additional payload is shown in Fig. 12c. During the initial experiments with the additional payload, we experienced overheating of the servomotors to the limit of 70 °C, for which the servomotor automatically shutdowns. Therefore, the maximum speed limit has been set to $v_x = 0.1\ \mathrm{ms^{-1}}$. After the speed adjustment, the robot with additional payload has been able to continuously walk for 53 minutes before the voltage on the battery dropped under 10.8 V. The temperature evolution for the additional payload is depicted in Fig. 12b.

The results indicate that the temperatures of the servomotors tend to be stable that also hold for the operational time, albeit the additional payload affects the maximum locomotion speed. Here, it is worth commenting that all the experiments have been done with the battery of the relatively small capacity 2600 mA h. Hence, it is expected that with the intended battery of 6000 mA h, which is only 1.35 times heavier than the utilized battery, which is about 70 g more, the projected robot operation time is far beyond one hour. Therefore, we can conclude the endurance evaluation results as supportive to the motivation of increasing the robot endurance despite additional servomotors in comparison to PhantomX AX robot utilized in our previous work [23], [29].

VI. CONCLUSION

In this work, we present HAntR, a novel six-legged walking robot with four degrees of freedom per leg. Based on the review of the existing hexapod walking platforms of similar size, we propose a new mechanical design of the robot that can utilize electronic actuators to negotiate rough terrains using only position feedback from the servomotors. The developed locomotion control strategy exhibit improved stability control when the AHRS unit is attached and thus enables the robot to walk on sloped surfaces. The mechanical design, together with the novel locomotion controller allowed us to build a relatively lightweight robotic platform that outperforms most of the similar six-legged platforms in speed and endurance, while it remains compact. The design choices of the developed HAntR are also built on five years of experience with PhantomX AX robot. HAntR is intended as the successor of the research platform not only in robotic information gathering in unstructured terrains but also in research on advanced locomotion control and object manipulation that are both enabled by the enhanced kinematic capabilities of HAntR. Since most of the current limitations of HAntR are caused by the utilized servomotors, which are, however, relatively inexpensive, the motion capabilities can be further improved using newer and more powerful actuators, e.g., such as Dynamixel X-series servomotors.

REFERENCES

[1] M. Raibert, K. Blankespoor, G. Nelson, and R. Playter, "BigDog, the Rough-Terrain Quadruped Robot," *IFAC Proceedings Volumes*, vol. 41, no. 2, pp. 10 822–10 825, 2008.

[2] H. Zhang, Y. Liu, J. Zhao, J. Chen, and J. Yan, "Development of a bionic hexapod robot for walking on unstructured terrain," *Journal of Bionic Engineering*, vol. 11, no. 2, pp. 176–187, Apr. 2014.

[3] T. M. Roehr, F. Cordes, and F. Kirchner, "Reconfigurable integrated multirobot exploration system (RIMRES): Heterogeneous modular reconfigurable robots for space exploration," *Journal of Field Robotics*, vol. 31, no. 1, pp. 3–34, 2014.

[4] D. Sanz-Merodio, E. Garcia, and P. Gonzalez-de Santos, "Analyzing energy-efficient configurations in hexapod robots for demining applica-

tions," *Industrial Robot: An International Journal*, vol. 39, no. 4, pp. 357–364, 2012.

[5] B. Kennedy, H. Aghazarian, Y. Cheng, M. Garrett, G. Hickey, T. Huntsberger, L. Magnone, C. Mahoney, A. Meyer, and J. Knight, "LEMUR: Legged excursion mechanical utility rover," *Autonomous Robots*, vol. 11, pp. 201–205, 2001.

[6] W. Xi, Y. Yesilevskiy, and C. D. Remy, "Selecting gaits for economical locomotion of legged robots," *International Journal of Robotics Research*, vol. 35, no. 9, pp. 1140–1154, 2016.

[7] M. Hutter, C. Gehring, D. Jud, A. Lauber, C. D. Bellicoso, V. Tsounis, J. Hwangbo, K. Bodie, P. Fankhauser, M. Bloesch, R. Diethelm, S. Bachmann, A. Melzer, and M. Hoepflinger, "ANYmal - a highly mobile and dynamic quadrupedal robot," in *IEEE/RSJ International Conference on Intelligent Robots and Systems (IROS)*, 2016, pp. 38–44.

[8] G. Bledt, M. J. Powell, B. Katz, J. Di Carlo, P. M. Wensing, and S. Kim, "MIT Cheetah 3: Design and Control of a Robust, Dynamic Quadruped Robot," in *IEEE/RSJ International Conference on Intelligent Robots and Systems (IROS)*, 2018, pp. 2245–2252.

[9] U. Saranli, M. Buehler, and D. E. Koditschek, "RHex: A simple and highly mobile hexapod robot," *International Journal of Robotics Research*, vol. 20, no. 7, pp. 616–631, 2001.

[10] B. Zhong, S. Zhang, M. Xu, Y. Zhou, T. Fang, and W. Li, "On a CPG-Based Hexapod Robot: AmphiHex-II With Variable Stiffness Legs," *IEEE/ASME Transactions on Mechatronics*, vol. 23, no. 2, pp. 542–551, 2018.

[11] F. Tedeschi and G. Carbone, "Design Issues for Hexapod Walking Robots," *Robotics*, vol. 3, no. 2, pp. 181–206, 2014.

[12] P. Gonzalez de Santos, E. Garcia, and J. Estremera, "Improving walking-robot performances by optimizing leg distribution," *Autonomous Robots*, vol. 23, no. 4, pp. 247–258, 2007.

[13] L. Frantsevich, "Optimal leg design in a hexapod walker," *Journal of Theoretical Biology*, vol. 175, no. 4, pp. 561–566, 1995.

[14] Y.-g. Zhu, B. Jin, W. Li, and S.-t. Li, "Optimal design of hexapod walking robot leg structure based on energy consumption and workspace," *Transactions of the Canadian Society for Mechanical Engineering*, vol. 38, no. 3, pp. 305–317, 2014.

[15] Z. Wang, X. Ding, A. Rovetta, and A. Giusti, "Mobility analysis of the typical gait of a radial symmetrical six-legged robot," *Mechatronics*, vol. 21, no. 7, pp. 1133–1146, 2011.

[16] D. Belter and P. Skrzypczyński, "Integrated Motion Planning for a Hexapod Robot Walking on Rough Terrain," *IFAC Proceedings Volumes*, vol. 44, no. 1, pp. 6918–6923, 2011.

[17] O. A. Silva, P. Sigel, W. Eaton, C. Osorio, E. Valdivia, N. Frois, and F. Vera, "CRABOT: A six-legged platform for environmental exploration and object manipulation," in *Proceedings of the 4th Congress on Robotics and Neuroscience*, no. 2312, 2018, pp. 46–51.

[18] Y. Liu, L. Ding, H. Gao, G. Liu, Z. Deng, and H. Yu, "Efficient force distribution algorithm for hexapod robot walking on uneven terrain," in *IEEE International Conference on Robotics and Biomimetics (ROBIO)*, 2016, pp. 432–437.

[19] S. S. Roy and D. K. Pratihar, "Effects of turning gait parameters on energy consumption and stability of a six-legged walking robot," *Robotics and Autonomous Systems*, vol. 60, no. 1, pp. 72–82, 2012.

[20] D. Grzelczyk, B. Stanczyk, and J. Awrejcewicz, "Kinematics, Dynamics and Power Consumption Analysis of the Hexapod Robot During Walking with Tripod Gait," *International Journal of Structural Stability and Dynamics*, vol. 17, no. 05, p. 1740010, 2017.

[21] H. Deng, G. Xin, G. Zhong, and M. Mistry, "Gait and trajectory rolling planning and control of hexapod robots for disaster rescue applications," *Robotics and Autonomous Systems*, vol. 95, pp. 13–24, 2017.

[22] S. S. Roy and D. K. Pratihar, "Kinematics, Dynamics and Power Consumption Analyses for Turning Motion of a Six-Legged Robot," *Journal of Intelligent & Robotic Systems*, vol. 74, no. 3-4, pp. 663–688, 2014.

[23] J. Faigl and P. Čížek, "Adaptive locomotion control of hexapod walking robot for traversing rough terrains with position feedback only," *Robotics and Autonomous Systems*, vol. 116, pp. 136–147, 2019.

[24] A. Roennau, G. Heppner, L. Pfotzer, and R. Dillmann, "LAURON V: Optimized leg configuration for the design of a bio-inspired walking robot," in *Nature-Inspired Mobile Robotics*, 2013, pp. 563–570.

[25] M. Bjelonic, N. Kottege, and P. Beckerle, "Proprioceptive control of an over-actuated hexapod robot in unstructured terrain," in *IEEE/RSJ International Conference on Intelligent Robots and Systems (IROS)*, 2016, pp. 2042–2049.

[26] B. H. Wilcox, T. Litwin, J. Biesiadecki, J. Matthews, M. Heverly, J. Morrison, J. Townsend, N. Ahmad, A. Sirota, and B. Cooper, "Athlete: A cargo handling and manipulation robot for the moon," *Journal of Field Robotics*, vol. 24, no. 5, pp. 421–434, 2007.

[27] D. Belter and K. Walas, "A compact walking robot–flexible research and development platform," in *Recent Advances in Automation, Robotics and Measuring Techniques*. Springer, 2014, pp. 343–352.

[28] D. Wettergreen, "Robotic walking in natural terrain," Ph.D. dissertation, Carnegie Mellon University, 1995.

[29] M. Prágr, P. Čížek, and J. Faigl, "Online incremental learning of the terrain traversal cost in autonomous exploration," in *Robotics: Science and Systems (RSS)*, 2019.

[30] J. Bayer and J. Faigl, "On autonomous spatial exploration with small hexapod walking robot using tracking camera Intel RealSense T265," in *European Conference on Mobile Robots (ECMR)*, 2019, pp. 1–6.

[31] C. Li, A. Pullin, D. Haldane, H. K Lam, R. S Fearing, and R. J Full, "Terradynamically streamlined shapes in animals and robots enhance traversability through densely cluttered terrain," *Bioinspiration & Biomimetics*, vol. 10, 2015.

[32] H. Zhuang, H. Gao, Z. Deng, L. Ding, and Z. Liu, "A review of heavy-duty legged robots," *Science China Technological Sciences*, vol. 57, no. 2, pp. 298–314, 2014.

[33] B. H. Jun, H. Shim, B. Kim, J. Y. Park, H. Baek, S. Yoo, and P. M. Lee, "Development of seabed walking robot CR200," in *OCEANS MTS/IEEE Bergen: The Challenges of the Northern Dimension*, 2013, pp. 1–5.

[34] M. Pitchai, X. Xiong, M. Thor, P. Billeschou, P. L. Mailänder, B. Leung, T. Kulvicius, and P. Manoonpong, "Cpg driven rbf network control with reinforcement learning for gait optimization of a dung beetle-like robot," in *International Conference on Artificial Neural Networks (ICANN)*, 2019, pp. 698–710.

[35] M. Gorner, T. Wimbock, A. Baumann, M. Fuchs, T. Bahls, M. Grebenstein, C. Borst, J. Butterfass, and G. Hirzinger, "The DLR-Crawler: A testbed for actively compliant hexapod walking based on the fingers of DLR-Hand II," in *IEEE/RSJ International Conference on Intelligent Robots and Systems (IROS)*, 2008, pp. 1525–1531.

[36] W. Cheah, H. H. Khalili, F. Arvin, P. Green, S. Watson, and B. Lennox, "Advanced motions for hexapods," *International Journal of Advanced Robotic Systems*, vol. 16, no. 2, p. 1729881419841537, 2019.

[37] M. Thor, J. C. Larsen, and P. Manoonpong, "Morf – modular robot framework," in *Proceedings of 2nd International Youth Conference on Bionic Engineering (IYCBE)*, 2018, pp. 23–25.

[38] S. Kalouche, D. Rollinson, and H. Choset, "Modularity for maximum mobility and manipulation: Control of a reconfigurable legged robot with series-elastic actuators," in *IEEE International Symposium on Safety, Security, and Rescue Robotics (SSRR)*, 2015, pp. 1–8.

[39] Trossen Robotics, "(@Online)," https://www.trossenrobotics.com/phantomx-ax-hexapod.aspx, 2020, cited on 2020-10-20.

[40] K. Halvorsen, "(@Online) Zenta robotic creations," http://zentasrobots.com, 2020, cited on 2020-10-20.

[41] HEBI Robotics, "(@Online)," http://docs.hebi.us/resources/kits/assyInstructions/A-2049-01_Data_Sheet.pdf, 2020, cited on 2020-10-20.

[42] A. Roennau, G. Heppner, M. Nowicki, and R. Dillmann, "LAURON V: A versatile six-legged walking robot with advanced maneuverability," in *IEEE/ASME International Conference on Advanced Intelligent Mechatronics*, 2014, pp. 82–87.

[43] K. Galloway, G. Clark Haynes, D. Ilhan, A. M Johnson, R. Knopf, G. A. Lynch, B. N Plotnick, M. White, and D. Koditschek, "X-rhex: A highly mobile hexapedal robot for sensorimotor tasks," University of Pennsylvania, Tech. Rep., 2010, technical Reports (ESE).

[44] D. Belter, "Efficient modeling and evaluation of constraints in path planning for multi-legged walking robots," *IEEE Access*, vol. 7, pp. 107 845–107 862, 2019.

[45] M. Bjelonic, N. Kottege, T. Homberger, P. Borges, P. Beckerle, and M. Chli, "Weaver: Hexapod robot for autonomous navigation on unstructured terrain," *Journal of Field Robotics*, vol. 35, no. 7, pp. 1063–1079, 2018.

[46] M. Thor, "Morf – modular robot framework," Master's thesis, The Maersk Mc-Kinney Moller Institute, University of Southern Denmark, 2019.

[47] A. J. Ijspeert, "Central pattern generators for locomotion control in animals and robots: A review," *Neural Networks*, vol. 21, no. 4, pp. 642–653, 2008.

[48] S. Aoi, P. Manoonpong, Y. Ambe, F. Matsuno, and F. Wörgötter, "Adaptive control strategies for interlimb coordination in legged robots: A review," *Frontiers in Neurorobotics*, vol. 11, p. 39, 2017.

[49] K. Walas, "Tactile sensing for ground classification," *Journal of Automation, Mobile Robotics & Intelligent Systems*, vol. 7, no. 2, pp. 18–23, 2013.
[50] M. Travers, J. Whitman, and H. Choset, "Shape-based coordination in locomotion control," *International Journal of Robotics Research*, vol. 37, no. 10, pp. 1253–1268, 2018.
[51] S. Kaliyamoorthy, R. D. Quinn, and S. N. Zill, "Force sensors in hexapod locomotion," *International Journal of Robotics Research*, vol. 24, no. 7, pp. 563–574, 2005.
[52] B. Tam, F. Talbot, R. Steindl, A. Elfes, and N. Kottege, "Openshc: A versatile multilegged robot controller," 2020.
[53] P. Arena, P. Furia, L. Patané, and M. Pollino, "Fly-inspired sensory feedback in a reaction-diffusion neural system for locomotion control in a hexapod robot," in *International Joint Conference on Neural Networks (IJCNN)*, 2015, pp. 1–8.
[54] T. Horvat, K. Karakasiliotis, K. Melo, L. Fleury, R. Thandiackal, and A. J. Ijspeert, "Inverse kinematics and reflex based controller for body-limb coordination of a salamander-like robot walking on uneven terrain," in *IEEE/RSJ International Conference on Intelligent Robots and Systems (IROS)*, 2015, pp. 195–201.
[55] J. Chen, Z. Liang, Y. Zhu, and J. Zhao, "Improving kinematic flexibility and walking performance of a six-legged robot by rationally designing leg morphology," *Journal of Bionic Engineering*, vol. 16, no. 4, pp. 608–620, 2019.
[56] B. Siciliano, L. Sciavicco, L. Villani, and G. Oriolo, *Robotics: Modelling, Planning and Control*. Springer Science & Business Media, 2010.
[57] M. R. Fielding and G. R. Dunlop, "Omnidirectional hexapod walking and efficient gaits using restrictedness," *International Journal of Robotics Research*, vol. 23, no. 10-11, pp. 1105–1110, 2004.
[58] P. Čížek and J. Faigl, "On locomotion control using position feedback only in traversing rough terrains with hexapod crawling robot," *IOP Conference Series: Materials Science and Engineering*, vol. 428, p. 012065, 2018.
[59] N. Kottege, C. Parkinson, P. Moghadam, A. Elfes, and S. P. N. Singh, "Energetics-informed hexapod gait transitions across terrains," in *IEEE International Conference on Robotics and Automation (ICRA)*, 2015, pp. 5140–5147.
[60] P. Čížek, D. Masri, and J. Faigl, "Foothold placement planning with a hexapod crawling robot," in *IEEE/RSJ International Conference on Intelligent Robots and Systems (IROS)*, 2017, pp. 4096–4101.
[61] S. Gottschalk, M. C. Lin, and D. Manocha, "OBB-Tree: A hierarchical structure for rapid interference detection," in *ACM Conference on Computer Graphics and Interactive Techniques (SIGGRAPH)*, 1996, pp. 171–180.

PETR ČÍŽEK received the Bc. and Ing. degrees in robotics and cybernetics from the Czech Technical University in Prague (CTU), Prague, Czech Republic, in 2013 and 2015, respectively. He is currently pursuing his Ph.D. degree in computer science with the Computational Robotics Laboratory, Artificial Intelligence Center, FEE, CTU. His research interests are multi-legged walking robots and their locomotion control, and efficient computation on FPGAs.

MARTIN ZOULA received the Bc. degree in robotics and cybernetics from the Czech Technical University in Prague (CTU), Prague, Czech Republic, in 2019. He is currently pursuing his Ing. degree in computer science at the FEE, CTU. His research interests are multi-legged walking robots and wireless communications in multi-robot teams.

JAN FAIGL is a full professor of computer science at the Faculty of Electrical Engineering (FEE), Czech Technical University in Prague (CTU). He received his Ph.D. (2010) in Artificial Intelligence and Biocybernetics and Ing. (2003) in Cybernetics from CTU. In 2013/2014, he was Fulbright visit scholar at the University of Southern California. He has been awarded the Antonin Svoboda Award from the Czech Society for Cybernetics and Informatics in 2011. He served as the guest editor of the special issue on "Online decision making in Multi-Robot Coordination" in Autonomous Robots journal.

He currently serves as the associate editor of the IEEE Transactions on Automation Science and Engineering (T-ASE). Since 2013, he is leading the Computational Robotics Laboratory (http://comrob.fel.cvut.cz) within the Artificial Intelligence Center (http://aic.fel.cvut.cz). He is also co-founder of the Center for Robotics and Autonomous Systems (http://robotics.fel.cvut.cz). His current research interests include combinatorial motion planning, robotic information gathering, long-term autonomous missions with online incremental learning, autonomous navigation, aerial systems, and multi-legged locomotion control.